Development of Iron-Doped Silicon Nanoparticles As Bimodal Imaging Agents

Mani P. Singh,[†] Tonya M. Atkins,[†] Elayaraja Muthuswamy,[†] Saeed Kamali,[†] Chuqiao Tu,[‡] Angelique Y. Louie,[‡] and Susan M. Kauzlarich[†,*]

[†]Department of Chemistry and [‡]Department of Biomedical Engineering, University of California, One Shields Avenue, Davis, California 95616, United States

ABSTRACT

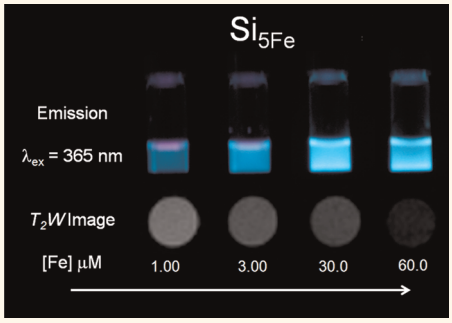

We demonstrate the synthesis of water-soluble allylamine-terminated Fe-doped Si (Si_{xFe}) nanoparticles as bimodal agents for optical and magnetic imaging. The preparation involves the synthesis of a single-source iron-containing precursor, Na_4Si_4 with *x*% Fe ($x = 1, 5, 10$), and its subsequent reaction with NH_4Br to produce hydrogen-terminated Si_{xFe} nanoparticles. The hydrogen-capped nanoparticles are further terminated with allylamine *via* thermal hydrosilylation. Transmission electron microscopy indicates that the average particle diameter is $\sim 3.0 \pm 1.0$ nm. The Si_{5Fe} nanoparticles show strong photoluminescence quantum yield in water ($\sim$10%) with significant T_2 contrast (r_2/r_1 value of 4.31). Electron paramagnetic resonance and Mössbauer spectroscopies indicate that iron in the nanoparticles is in the +3 oxidation state. Analysis of cytotoxicity using the resazurin assay on HepG2 liver cells indicates that the particles have minimal toxicity.

KEYWORDS: silicon nanoparticles · water-soluble · thermal hydrosilylation bimodal imaging agents · iron doping · hepatocytes · cytotoxicity · resazurin assay

The research in the area of nanotechnology has seen immense progress over the years. It is highly exploratory, driven by the demand for better materials for applications in electronics, sensors, catalysis, and biomedical science for diagnostics and therapeutics.[1−5] The vast applicability of nanoparticles is a result of their (i) small size, which gives them a high surface to volume ratio, (ii) highly tailorable physical properties such as absorbance, emission, and magnetism, (iii) chemically active surface, and (iv) ability to form highly stable structures.[2] A combination of all the above-mentioned properties has led to the application of nanoparticles for diagnostics and therapeutics including metal nanoparticles (Au, Ag),[6,7] semiconductor nanoparticles (II−VI, III−V, Si),[1,2,8] and magnetic nanoparticles (Fe_3O_4, FeCo alloy, MnO, Gd_2O_3).[9−11]

Imaging is an important diagnostic technique, and some of the most clinically relevant modalities include optical imaging, MRI (magnetic resonance imaging), and PET (positron electron tomography).[12] While all the imaging techniques have strengths as diagnostics methods, they all suffer from some disadvantages. Optical imaging suffers from low resolution *in vivo* (2−3 mm) along with limited skin/tissue penetration (<1 cm), while MRI suffers from low sensitivity (mM−μM).[13−15] Multimodality allows for combining the advantages of multiple imaging modalities and may help to overcome the shortcomings of the involved techniques.[13−16] Combining fluorescence and magnetic resonance imaging provides the high sensitivity of optical imaging (nM−pM) and high tissue penetration of MR imaging (no limit).[13,15] The ability to exploit the multiple modalities in a single imaging agent makes the measurement more accurate and, thus, the diagnosis and/or treatment more reliable.[17]

Although it is challenging to blend multiple modalities into a single entity, multimodal nanoparticles offer hope in achieving this goal. The fluorescent properties of semiconductor nanoparticles have proven to be useful for optical imaging, while the magnetic properties of iron oxide nanoparticles have been applied for magnetic resonance imaging; it is attractive to consider blending these materials into a single particle.[12,14] There are examples of multimodal imaging agents available in the literature with focus on the development of

* Address correspondence to smkauzlarich@ucdavis.edu.

Received for review April 6, 2012 and accepted May 22, 2012.

Published online May 22, 2012
10.1021/nn301536n

magneto-fluorescent bimodal imaging agents either by conjugating a fluorescent label to magnetic particles[18,19] or by conjugating a MR-active probe to a fluorescent semiconductor nanoparticle.[12,20] While these probes have shown success for dual mode imaging, there is concern that the chemically conjugated label can be released, especially under *in vivo* conditions, and mar image interpretation due to the presence of free label. Another approach to designing bimodal imaging agents is to dope a MR-active probe into the nanoparticle.[21,22] This single-entity approach resolves the problems associated with the possible labile nature of chemically bonded groups. Reports have shown successful doping of metal ions into fluorescent semiconductor nanoparticles.[21−23] One factor that weighs into the development of any new material for biological applications is its toxicity, both biological and environmental.[24]

Silicon nanoparticles, which are relatively new in the area of bioimaging,[25−29] offer a good alternative to the traditional nanoparticles, as the silicon-based materials have been shown to exhibit minimal toxicity.[25,30−33] They exhibit a stable fluorescence at different wavelengths based on the synthetic route. They can be synthesized by a variety of methods reported in the literature ranging from reduction of silicon halides,[34] to plasma synthesis,[35] high-temperature annealing of SiO_x followed by HF etching,[36] electrothermal dispersion of bulk silicon,[25] and microwave-assisted reaction of Zintl phases.[37] All the above-mentioned synthetic routes produce stable silicon nanoparticles; however many produce nanoparticles that are hydrophobic, which makes them unfavorable for bioimaging unless they can be modified to be water-soluble. The reaction of the Zintl phase Na_4Si_4 either in a traditional thermal[38−40] or in a microwave reactor[37] produces hydrogen-capped silicon nanoparticles that can be further reacted to produce water-soluble nanoparticles. The benefits of using a Zintl salt to prepare nanoparticles are that it is possible to add paramagnetic ions as a dopant to the starting material and incorporate both photoluminescence and paramagnetism into one small entity. We have reported the synthesis of water-soluble manganese-doped silicon nanoparticles and shown that both photoluminescence and MRI detection is possible.[26]

In this article, we expand on our previous work and further develop this approach to synthesize highly stable and photoluminescent water-soluble propylamine-terminated, iron-doped silicon (Si_{xFe}) nanoparticles and demonstrate their application as potential bimodal imaging agents. The nanoparticles were synthesized from *x*Fe:Na_4Si_4, which acts as a single-source precursor to obtain the desired nanoparticles. The nanoparticles were characterized by a variety of techniques to assess their physical characteristics including core size, fluorescence, electron paramagnetic resonance (EPR), oxidation state of the dopant, relaxivity, and magnetic resonance imaging. The nanoparticles were examined for their toxicity on HepG2 cells and compared to undoped silicon (Si) nanoparticles.

TABLE 1. Particle Size (diameter), Quantum Yield (QY), and Iron Content (mol %) for Si_{xFe} Nanoparticles Dispersed in Nanopure Water

sample	particle size (nm)	QY (%)	Fe content (mol %)
Si_{1Fe}	2.91 ± 0.99	15.0 ± 1.00	0.60 ± 0.20
Si_{5Fe}	2.87 ± 1.21	10.0 ± 1.50	0.90 ± 0.10
Si_{10Fe}	3.01 ± 1.10	1.00 ± 0.05	0.50 ± 0.15

RESULTS AND DISCUSSION

The precursors *x*Fe:Na_4Si_4 and the amine-terminated iron-doped silicon nanoparticles (Si_{xFe}) were synthesized in a similar fashion to what we previously described for Mn-doped silicon nanoparticles.[26] The reaction between the precursor *x*Fe:Na_4Si_4 and NH_4Br in DMF produced hydrogen-terminated nanoparticles, which could easily hydrolyze if exposed to air and/or water and hence are not very stable. It is important to coat them with a ligand, which will enhance their stability to air and water. Hydrosilylation has been utilized over the years to stabilize hydrogen-terminated silicon surfaces in nanoparticles and thin layers.[34] An unsaturated hydrocarbon (with an additional functional group or otherwise) can replace the surface hydrogen, forming a stable Si−C bond, thus protecting the surface from hydroxylation. Hydrosilylation has been reported to be catalytically,[29,41,42] thermally,[43] or photolytically[29,44] driven. The thermally assisted method is advantageous over the other routes, as it avoids extra purification steps (as in the case of catalytic methods) or the longer reaction times[42] (as in the case of UV-assisted methods). Allylamine is a short-chain ligand that can help maintain a smaller hydrodynamic size for further applications.[45] The absence of a long carbon chain also assists in high water solubility, and the terminal amine group lends a wide range of functionality to the nanoparticles for further conjugation to molecules including but not limited to nucleic acids, peptides, and therapeutic agents. The amine-terminated Si_{xFe} particles prepared by this route are extremely stable to light, air, and water over a period of time. Over a period of 15 months, nanoparticles prepared *via* this synthetic route when stored in water on a benchtop do not fall out of solution and exhibit a 75% loss in overall quantum yield in comparison to a freshly prepared sample (Figure S1). The synthesis is highly reproducible with the average core size for Si_{xFe} of ∼3−4 nm, as determined by TEM (Table 1). A typical TEM image for Si_{5Fe} is shown in Figure 1. Figure 1a shows the average size of the Si_{5Fe} nanoparticles, and Figure 1b is the high-resolution TEM image of Si_{5Fe} nanoparticle wherein

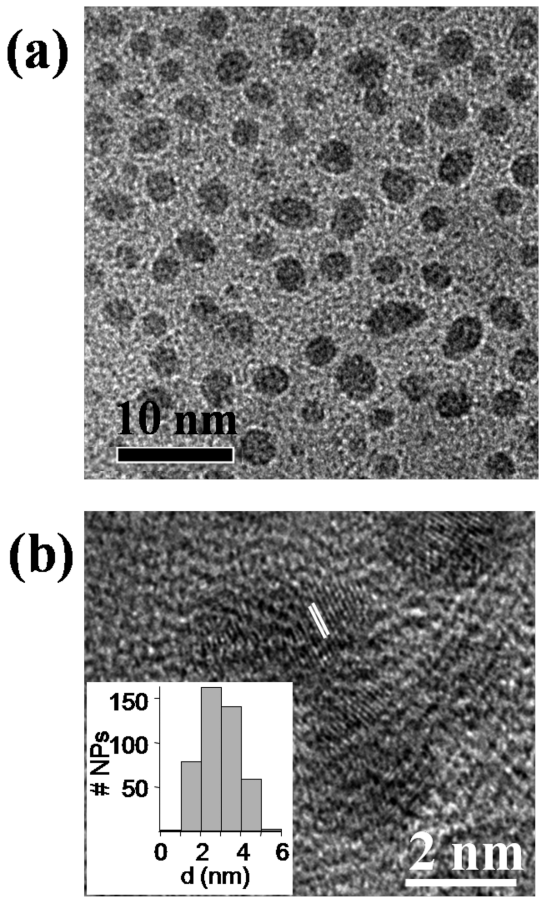

Figure 1. (a) TEM image of Si_{5Fe} and (b) (2 2 0) Si plane in the nanoparticles with the measured distance between the planes in the nanoparticles being 1.9 Å. Inset in (b) depicts the size distribution of the Si_{5Fe} nanoparticles as measured by TEM.

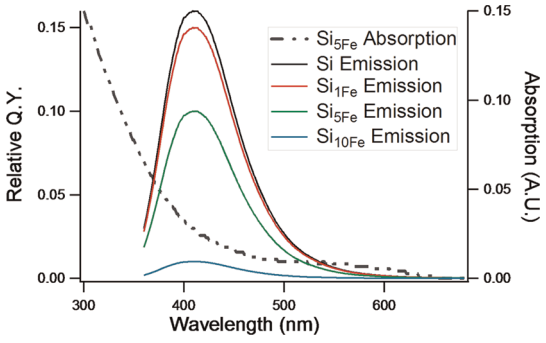

Figure 2. Relative quantum yield (QY) for amine-terminated water-soluble Si and Si_{xFe} nanoparticles. The absorption spectrum for Si_{5Fe} is shown as well. Si, Si_{1Fe}, and Si_{10Fe} nanoparticles exhibit a similar absorption profile.

the (2 2 0) lattice plane (1.9 Å) for silicon can be seen as indicated. The inset in Figure 1b depicts the size distribution of the Si_{5Fe} nanoparticles. The high-resolution TEM (HRTEM) images confirm the absence of any independent Fe and Si nanoparticles or Fe–Si core–shell structure for these nanoparticles, as the difference in the densities of silicon and iron would have been clearly visible in a high-resolution TEM image.

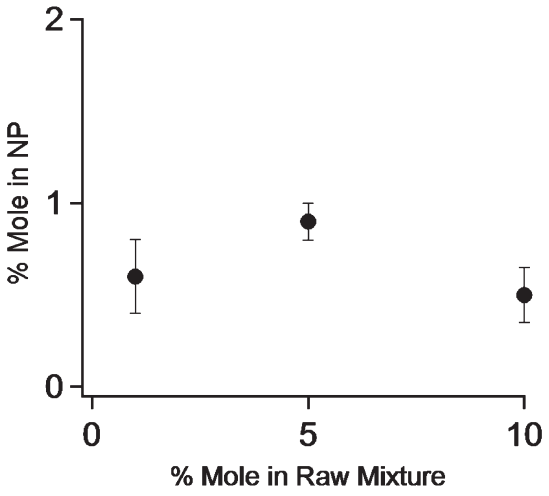

Figure 3. Plot of the amount of dopant (Fe^{3+}) in the Si_{xFe} nanoparticles *vs* the amount of Fe^{3+} in the initial milled mixture (n = 3).

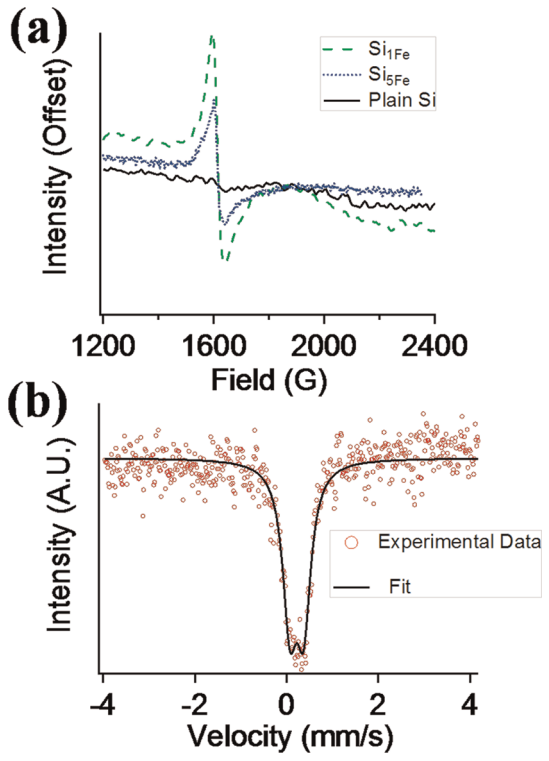

Figure 4. (a) X-band EPR spectra for Si_{1Fe} (dashed line) and Si_{5Fe} (dotted line). For comparison, the EPR spectrum for undoped silicon nanoparticles is also included (solid line). (b) Mössbauer spectrum of Si_{5Fe} nanoparticles fits the parameters specific to Fe^{3+}.

The photophysical characteristics of the nanoparticles were measured in aqueous solution. The UV–vis spectra for the nanoparticles show no significant absorption at wavelengths longer than 600 nm. The photoluminescence (PL) was measured with λ_{ex} = 350 nm for all the samples and yielded an emission peak centered at 430 nm (λ_{em} = 430 nm), as shown in Figure 2. The highest quantum yield of 15% was

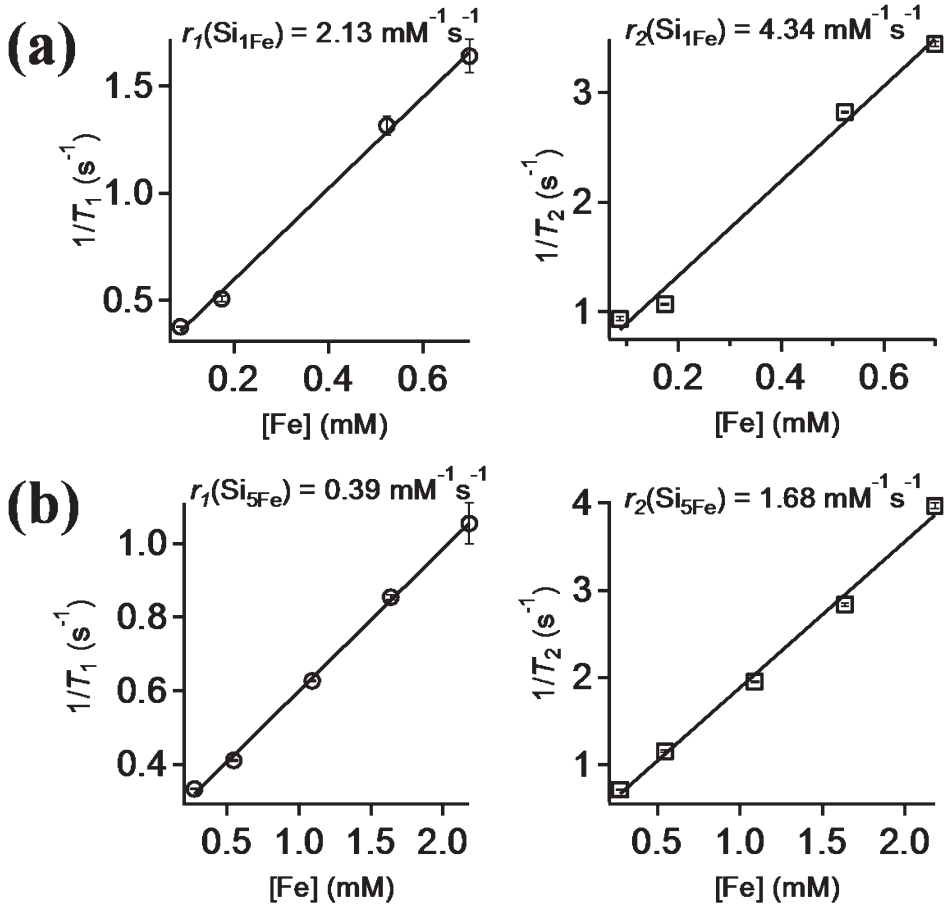

Figure 5. Relaxivity plots for (a) Si_{1Fe} and (b) Si_{5Fe} dissolved in water and measured at 37 °C (n = 3).

observed for the sample with the smallest amount of Fe, x = 1, while the sample with x = 5 had a quantum yield of 10%. At x = 10, the quantum yield went down to 1% (Table 1). Loss of quantum yield is not beneficial for the development of a multimodal agent; therefore no magnetic measurements or toxicity assays were performed on the Si_{10Fe} nanoparticles.

Quantitative elemental analysis was performed to determine the extent of iron doping into the nanoparticles. The amount of $Fe(acac)_3$ was increased consistently in the starting mixture with the expectation of achieving higher amounts of iron doping in the nanoparticles. However, analysis of the inductively coupled plasma mass spectrometry (ICP-MS) data indicated that even at the highest amount of $Fe(acac)_3$ in the starting mixture, the iron incorporation into the nanoparticles did not exceed ~1% (Figure 3, Table 1). This observation is indicative of an upper limit to doping levels in the silicon nanoparticle system, and one can hypothesize that the nanoparticle extrudes dopant species in excess of ~1%, thus relieving itself of excess strain in the Si nanoparticle structure. As mentioned in the Experimental Section, the reaction between xFe:Na_4Si_4 and NH_4Br produces a yellow solution that contains the soluble nanoparticles and a black precipitate. As the nanoparticles did not show any increase in the iron content with increasing x, the black precipitate (byproduct) was analyzed by powder XRD. The powder X-ray diffraction (XRD) pattern for the Si_{10Fe} byproduct had diffraction peaks corresponding to NaBr, Si, FeSi, and Fe, whereas that for Si_{1Fe} did not (Figure S2). The Si_{5Fe} sample showed a small peak attributed to FeSi, but no evidence for Fe. These results support the hypothesis that only a limited amount of Fe is soluble in the 3 nm diameter silicon nanoparticles.

Figure 4a shows the X-band EPR spectrum of the amine-terminated Si_{1Fe} and Si_{5Fe} nanoparticles measured at 10 K. Figure 4a also includes the EPR spectrum for amine-terminated undoped silicon nanoparticles for comparison. The singlet at g = 4.3 observed in the case of both Si_{1Fe} and Si_{5Fe} is indicative of isolated high-spin Fe(III) centers under rhombic distortion.[46−48] Although there have not been any reports on EPR studies of iron doping into nanoparticles, there are several EPR reports on iron centers trapped in the various glasses, amino acid crystals, and zeolite structures.[49−52] On the basis of these reports it can be concluded that there are isolated iron centers in the +3 oxidation state in the core of the nanoparticle. A full sweep EPR spectrum for the undoped silicon nanoparticles and Si_{5Fe} is shown in the Supporting Information (Figure S3). This result is consistent with the iron center

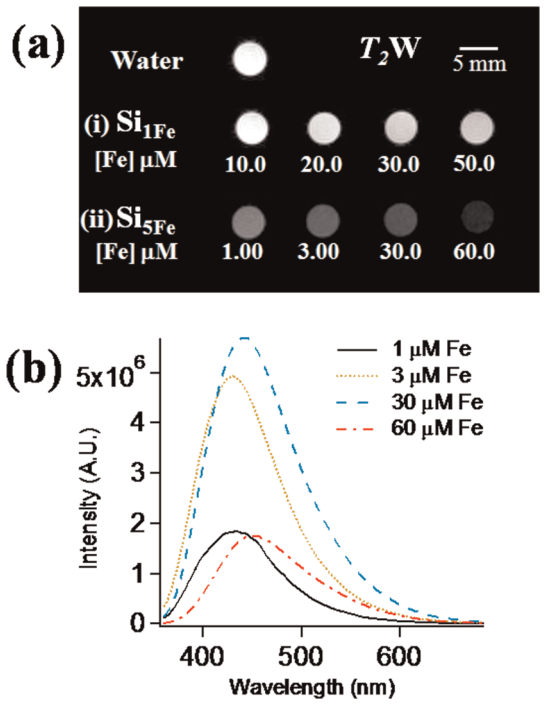

Figure 6. (a) T_2-weighted MRI images for (i) Si_{1Fe} and (ii) Si_{5Fe} nanoparticles dissolved in water. (b) Emission intensity of the same Si_{5Fe} samples from (a) measured at $\lambda_{ex} = 350$ nm.

as an isolated dopant within the nanoparticle structure and also indicates that there were no clusters of iron in the structure. This result corroborates the absence of core−shell-like structures for these nanoparticles, as was clearly seen in the HRTEM images (Figure 2).

To further probe the oxidation state of the iron centers in the nanoparticles, ^{57}Fe Mössbauer spectroscopy was carried out on Si_{5Fe} dispersed in ethanol. Mossbauer spectroscopy is a much more sensitive technique and can distinguish between the +2 and +3 states of iron with more accuracy than EPR spectroscopy, as the EPR signal for Fe^{2+} is very weak and difficult to detect. The spectrum was least-squared fit using Recoil software,[53] and the centroid shift is reported with respect to metallic α-iron at room temperature (Figure 4b). The parameters from the fitting are the centroid shift ($\delta = 0.22 \pm 0.01$ mm/s), quadrupole splitting ($\varepsilon = 0.30 \pm 0.01$ mm/s), and the Lorentzian line width ($\Gamma = 0.38 \pm 0.01$ mm/s).[54] These parameters are in good agreement with Fe^{3+}, indicating 3+ is the only oxidation state for the iron present in the nanoparticles.

The relaxivity measurements were carried out on Si_{1Fe} and Si_{5Fe} at 37 °C (1.4 T) and are shown in Figure 5. The r_2/r_1 for Si_{1Fe} was calculated to be 2.04, while that for Si_{5Fe} was 4.31. For these nanoparticles to be useful as bimodal imaging agents, along with a measurable quantum yield, they should also act as good MRI contrast agents. Magnetic resonance imaging experiments were carried out on Si_{1Fe} (QY = 15%) and Si_{5Fe} (QY = 10%). Figure 6a shows the T_2-weighted images

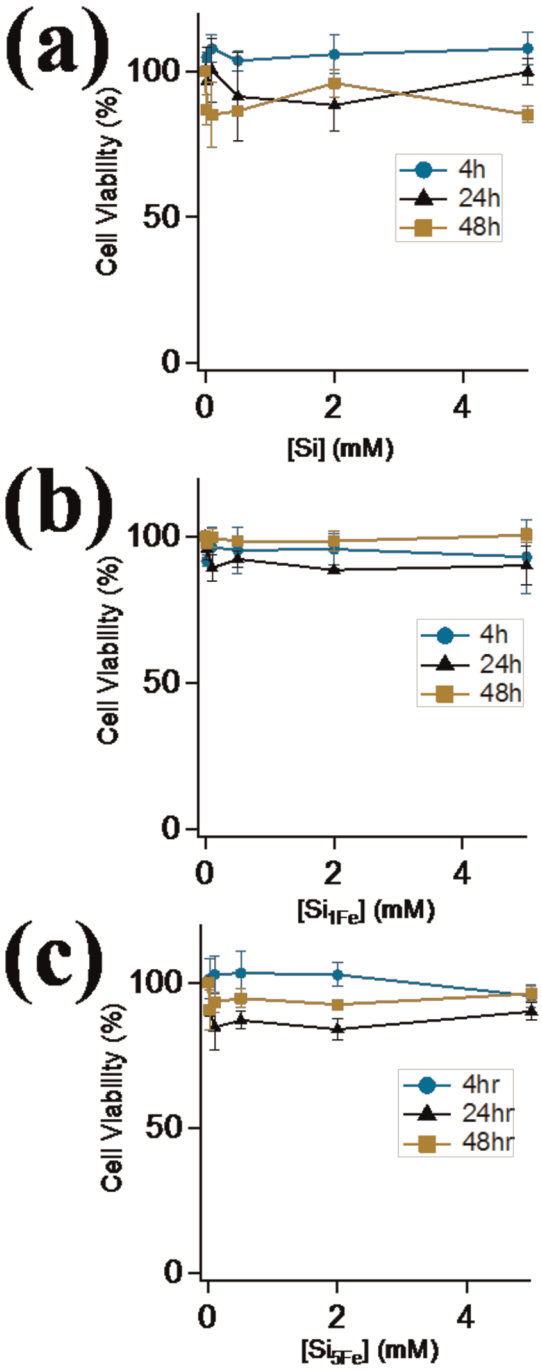

Figure 7. Cell viability for HepG2 cells when incubated with amine-terminated (a) undoped Si, (b) Si_{1Fe}, and (c) Si_{5Fe} nanoparticles at concentrations ranging from 0 to 5.0 mM for 4, 24, and 48 h ($n = 3$). At the highest concentrations with longest incubation times the cells exhibit ≥85% viability.

for both Si_{1Fe} and Si_{5Fe} nanoparticles dissolved in water. The Si_{5Fe} samples produce a high contrast even at concentrations as low as 1.0 μM, whereas Si_{1Fe} did not produce any notable contrast, as shown in Figure 6a. Neither of the nanoparticle samples produced noticeable T_1 contrast (data not shown).

The optical emission intensity of the Si_{5Fe} samples was measured at the same iron concentration as for the MRI studied. The samples were excited at $\lambda_{ex} = 350$ nm,

and as the samples entered the nonlinear region of absorption at higher concentration, the λ_{max} of emission red-shifted with the highest concentration sample (60 μM Fe) to 450 nm (Figure 6b). A plot of the area under the emission intensity curve as a function of concentration and emission λ_{max} as a function of concentration are presented in the Supporting Information (Figure S4). This shows a quenching of emission intensity and energy shift in the λ_{em} as a function of concentration of nanoparticles. Organic fluorophores are known to exhibit changes in their photophysical properties as a result of stacking or aggregation.[55,56] Similar effects have been observed with other fluorescent semiconductor nanoparticles as well to develop switchable fluorescent probes.[57] The change in the λ_{max} for silicon nanoparticles at higher concentration can be applied to confirm the delivery of a payload at a certain site.

Some of the most important criteria that any new material developed for biological applications (including imaging) must fulfill are biocompatibility, low toxicity, and biodegradability. Various silicon structures have been reported to be highly biocompatible[31,33] and are known to degrade to orthosilicic acid, $Si(OH)_4$, which can be easily excreted out of the body.[25,31] However, because nanoparticulates typically are cleared through the liver, retention in the liver is of concern for possible toxicity as the particles degrade.[25,58] Therefore, it is very important to study the effect of these particles on liver cells. HepG2 cells were treated with different concentrations (0−5 mM) of amine-terminated Si_{1Fe} and Si_{5Fe} for 4, 24, and 48 h. Similar experiments were repeated with amine-terminated undoped silicon nanoparticles to compare the effect of dopant. The cell viability was measured using a resazurin assay. The assay is composed of the resazurin dye, which is nonfluorescent by itself; however, it is reduced to its fluorescent form in the presence of live cells. The cell viability for HepG2 cells treated with Si, Si_{1Fe}, and Si_{5Fe} nanoparticles is presented in Figure 7. The nanoparticles show minimal toxicity (cell viability ≥85%) to the HepG2 cells throughout the concentration range even at the longest incubation times. Statistical evaluation of the survival rates for the hepatocytes indicates that the survival at 24 and 48 h is statistically significant ($p < 0.05$) in comparison to 4 h incubation times, whereas the difference is not significant ($p > 0.05$) when comparing the difference in survival rates at 24 and 48 h incubation times. We have previously shown that the nanoparticles can be detected by imaging after uptake by macrophages.[26] Some previous studies have shown that the amine-terminated silicon nanoparticles can have *in vitro* toxic effects, including an increase in the production of intracellular reactive oxygen species measured by a series of complex assays.[33,59] Resazurin assay is a relatively simple assay to measure the cytotoxicity and to completely understand the toxicological effects detailed, and more complex cell viability assays need to be employed for these nanoparticles. A detailed analysis to assess the cytotoxicity of these nanoparticles is in progress.

CONCLUSIONS

Iron-doped silicon nanoparticles (Si_{xFe}) have been successfully synthesized from the iron-doped sodium silicide precursor (xFe:Na_4Si_4). These nanoparticles exhibit extreme stability toward light, air, and water. Higher concentrations of the iron dopant in the initial mixture led to extreme loss of photoluminescence; however, at lower concentrations (x = 5%), the nanoparticles were bright and also produced a significant T_2 contrast. These nanoparticles were also of low toxicity, as seen in the cell viability assays with cell viability ≥85% at concentrations as high as 5 mM. These nanoparticles are promising for bioimaging applications, and the presence of free amines on the surface makes them highly applicable for targeted drug delivery as well. Future work on these nanoparticles is focused on bioconjugation and an assessment of the toxicity effects of these nanoparticles on other cell lines. These studies will help substantiate the overall minimal toxicity of the particle and also further the applicability of these particles for various other applications in diagnostics and therapeutics.

EXPERIMENTAL SECTION

Materials. Reagents for nanoparticle synthesis: sodium hydride powder (NaH, 95%), silicon powder (Si, 99%), anhydrous iron(III) acetylacetonate powder ($Fe(acac)_3$, 99.99%), allylamine ($C_3H_5NH_2$, 98%), ammonium bromide (NH_4Br, ≥99.99%), and *N*, *N*-dimethylformamide (DMF, 99.8%), were purchased from either Sigma Aldrich or Fisher Scientific. $Fe(acac)_3$ and NH_4Br were dried overnight in a vacuum oven. Allylamine (under N_2) and DMF (over sodium metal under vacuum) were distilled prior to use. Na_4Si_4 pellets were obtained from SiGNa Chemistry, Inc. The pellets were crushed to a powder using a mortar and pestle in a N_2-filled glovebox. Water was purified using a Nanopure analytical UV water system (18.0 MΩ cm, Barnstead). Reagents for cell culture: minimum essential medium (MEM) (1×), trypsin 0.05% (1×) with EDTA 4Na, MEM nonessential amino acid solution 10 mM (100×), penicillin−streptomycin (5000 units of penicillin (base) and 5000 μg of streptomycin (base)/mL), fetal bovine serum, Dulbecco's phosphate-buffered saline (D-PBS) (1×), and MEM sodium pyruvate solution 100 mM (100×), were purchased from Invitrogen, Inc. The cell vitality assay kit, C_{12}Resazurin/SYTOX Green, was also purchased from Invitrogen, Inc.

Preparation of xFe-Doped Silicon (Si_{xFe}) Nanoparticles (x = 1%, 5%, 10%). Fe-doped silicon nanoparticles were synthesized from the Fe-doped sodium silicide (xFe:Na_4Si_4) precursor following a previously published procedure.[26,60] The xFe:Na_4Si_4 precursors were prepared according to a modified procedure published for the synthesis of Na_4Si_4.[60] Briefly, mixtures of NaH, Si, and $Fe(acac)_3$ in different molar ratios (m_{NaH}:m_{Si}:m_{Fe} = 1.9:(1 − x):x, and x = 1%, 5%, 10%) were milled for 30 min in a high-energy Spex 8000 M mill

using a tungsten carbide milling vial (volume = 55 mL) and three tungsten carbide balls (one 11.2 mm and two 7.9 mm diameter). The milled mixture was placed in a N_2-filled glovebox and transferred to an alumina crucible. The crucible was covered with an alumina cover and placed in a quartz tube with stopcock adapters. The quartz tube was placed in a tube furnace and attached by means of the stopcock adapters to an argon flow at one end and a bubbler at the other. The apparatus was heated at 420 °C for 48 h followed by an additional 12 h at 500 °C under a constant flow of argon. The product was cooled to room temperature under flowing argon and transferred to the glovebox for further use and storage.

To synthesize the nanoparticles, 0.2 g of *x*Fe:Na_4Si_4 and 0.4 g of NH_4Br were added to a 250 mL Schlenk flask with a Teflon-coated stir bar in the N_2-filled glovebox. The flask was brought out of the glovebox and placed under N_2 on a Schlenk line. Then 100 mL of degassed DMF was cannulated into the flask, and the mixture was refluxed for 8−12 h in order to produce hydrogen-terminated Fe-doped silicon particles. The reaction was considered complete when there was no more ammonia gas indicated with a pH strip at the exit bubbler. The reaction mixture was then cooled to room temperature, 2 mL of degassed allylamine was added to the flask, and the reaction mixture was refluxed again for 4−6 h in order to produce propylamine-terminated nanoparticles *via* thermal hydrosilylation. The product, which was a yellow solution with a black precipitate, was cooled to room temperature and transferred to centrifuge tubes. The contents were centrifuged at 8000 rpm for 20 min. The yellow supernatant was transferred into a round-bottom flask, while the black precipitate was dried in a vacuum oven overnight for further characterization. The supernatant was evaporated using a Buchi rotary evaporator when 10 mL of Nanopure water (npH_2O) was added to the flask, and the solution evaporated again. This step was repeated to completely remove DMF (4 or 5 times) followed by addition of 10 mL of npH_2O.The solution was dialyzed against npH_2O for 2−4 h to remove any excess reagents and water-soluble impurities. The contents of the dialysis bag were then filtered using a 0.45 μm filter. The filtrate was brought to dryness using the rotary evaporator. The product was dissolved in 10 mL of npH_2O (or in DMF for EPR) and used for further characterization and experiments. Amine-terminated silicon nanoparticles (undoped) were synthesized and purified in a similar manner using Na_4Si_4 as the starting material.

CAUTION: NaH, Na_4Si_4, and xFe:Na_4Si_4 are highly reactive to air and moisture, hence must be handled under an inert atmosphere with care.

Characterization. The black precipitate from the Si_{xFe} nanoparticle syntheses was analyzed by powder X-ray diffraction on a Bruker D8 Advance X-ray diffractometer with Cu Kα radiation (λ = 1.54178 Å). The core size for the nanoparticles was determined by transmission electron microscopy on a JEOL 2500SE Schottky emitter microscope operating at 200 kV and equipped with a Gatan multiscan camera. TEM samples were prepared by dropping a methanol solution of the nanoparticle on a holey-carbon-coated, 400-mesh electron microscope grid and drying them under a lightbulb overnight. HRTEM images were collected on the same instrument, and the grids were prepared in a manner similar to that for the low-resolution image. Elemental analysis to determine the amount of iron doping in the nanoparticles was performed on ICP quadrupole mass spectrometers (Agilent Technologies 7500ce). Quantum yield measurements on an aqueous solution of nanoparticles were performed by measuring the photoluminescence spectra on a FluoroMax-3P fluorometer and UV−vis spectra on a Shimadzu UV-1700 PharmaSpec spectrometer. The quantum yields for Si_{xFe} particles are reported with respect to quinine sulfate standard dissolved in 0.1 M H_2SO_4 and excited at 350 nm.

Longitudinal (T_1) and transverse (T_2) relaxation times were measured at 60 MHz (1.4 T), pH 7.2, and 37 °C on a Bruker Minispec mq60 (Bruker, Billerica, MA, USA). The solutions of Si_{xFe} nanoparticles were prepared by dissolving the appropriate amount of samples in npH_2O. Each solution was incubated at 37 °C for 10 min before measurement. The longitudinal (r_1) and transverse (r_2) relaxivity were obtained by calculating the slope of the line for plots of $1/T_1$ *vs* [Fe] and $1/T_2$ *vs* [Fe], respectively. MRI was performed on a BrukerAvance I Console (400 MHz (9.4 T), 21 °C, Bruker, Billerica, MA, USA). For the T_1 measurements, TR = 1500 ms and TE = 8 ms, while for the T_2 measurements TR = 1000 ms and TE = 210 ms. The magnet was equipped with the standard gradient set (95 mT m^{-1} maximum gradient) and 30 mm internal diameter SAW volume coil made by M2M Imaging Corp. (Cleveland, OH, USA). For all images a flash-2D sequence was used with a field view of 3.2 × 3.2 cm^2, slice thickness 1.0 mm, and a 128 × 128 matrix.

The EPR spectra for the samples were collected on a Bruker ECS106 X-band spectrometer, equipped with an Oxford Instruments liquid helium cryostat. Typical experimental conditions were frequency 9.68 GHz, temperature 10 K, modulation amplitude 10 G, microwave power 0.50 m, conversion time 40.96 ms, time constant 40.96 ms, average of 10 scans. Samples were dissolved in DMF. ^{57}Fe Mössbauer spectroscopy was performed at 80 K using a SEE Co. MS4 spectrometer equipped with a Janis SVT-400 cryostat. The radioactive source was ^{57}Co in a Rh matrix maintained at room temperature. The Si_{5Fe} sample dissolved in DMF was poured into the sample cup and frozen under liquid N_2 to get a 2 mm thick sample for the measurement. The spectrum was least-squared fit using Recoil software,[53] and the values for metallic α-iron were used to report the centroid shift for the sample.

Toxicity Assay. Hepatic cells (HepG2 cells, from ATCC) were maintained in MEM supplemented with 10% FBS, 200 U/mL penicillin, 200 μg/mL streptomycin, 1 mM sodium pyruvate, and 1 mM nonessential amino acids at 37 °C in a humidified 5% CO_2 atmosphere. The cells were released from the culture flask using 0.05% trypsin and resuspended in 13 mL of supplemented MEM. A 10 μL portion of the suspension was loaded on a hemacytometer to determine the cell density. Appropriate dilution was carried out to obtain a cell density of 5 × 10^4 cell/mL of the suspension. Cells were plated into a 96-well plate at 200 μL of the cell suspension per well. Appropriate amounts of dried nanoparticles (Si_{xFe} or Si nanoparticles) were dissolved in supplemented MEM to get a stock solution with 5 mM silicon concentration as determined by ICP-MS. This molar concentration can be converted to g/L (mass/volume) by considering a 3 nm particle comprising a total of 963 silicon atoms and a 100% surface coverage (275 surface silicon atoms) by the propylamine ligand.[61] The cells in the well plate were incubated with the nanoparticle solution of 0, 0.02, 0.2, 0.5, and 5 mM concentrations for 4 h. The lower concentration [Si] solutions were prepared by serial dilution of the 5 mM stock solution. The cell viability was determined using a resazurin assay. For this, 5 mM resazurin solution was prepared in DMSO, which was further diluted to 5 μM using the supplemented MEM. For the 4 h time point the media was removed from each well and the cells were washed with 1× PBS (3 × 200 μL) followed by the addition of 200 μL of 5 μM resazurin solution to each well. The well plate was then placed on a Safire^2 monochromator microplate reader (Tecan Austria G.M.B.H., Austria), λ_{ex} = 563 nm and λ_{em} = 587 nm, to measure the fluorescence. The cell viability was assessed on the basis of the relative fluorescent signal in comparison to the control well. The same experiment was repeated for the 24 and 48 h time points for the cell viability.

Conflict of Interest: The authors declare no competing financial interest.

Acknowledgment. We recognize the support from NIH for funding this work through EB008576-01. We would like to thank Dr. J. H. Walton (UC Davis NMR Facility and CalEPR) for the MRI and EPR experiments and Prof. A. Revzin (Department of Biomedical Engineering, UC Davis) for supplying the HepG2 cells.

Supporting Information Available: pXRD patterns for the byproduct of nanoparticle synthesis, full sweep EPR spectrum, and information on the emission of nanoparticles as a function of time, concentration, and excitation wavelength. This material is available free of charge *via* the Internet at http://pubs.acs.org.

REFERENCES AND NOTES

1. Gao, X. H.; Cui, Y. Y.; Levenson, R. M.; Chung, L. W. K.; Nie, S. M. *In Vivo* Cancer Targeting and Imaging with

Semiconductor Quantum Dots. *Nat. Biotechnol.* **2004**, *22*, 969–976.
2. Alivisatos, P. The Use of Nanocrystals in Biological Detection. *Nat. Biotechnol.* **2004**, *22*, 47–52.
3. Tao, A. R.; Habas, S.; Yang, P. D. Shape Control of Colloidal Metal Nanocrystals. *Small* **2008**, *4*, 310–325.
4. Astruc, D.; Lu, F.; Aranzaes, J. R. Nanoparticles as Recyclable Catalysts: The Frontier between Homogeneous and Heterogeneous Catalysis. *Angew. Chem., Int. Ed.* **2005**, *44*, 7852–7872.
5. Shipway, A. N.; Katz, E.; Willner, I. Nanoparticle Arrays on Surfaces for Electronic, Optical, and Sensor Aapplications. *Chem. Phys. Chem.* **2000**, *1*, 18–52.
6. Huang, X. H.; Jain, P. K.; El-Sayed, I. H.; El-Sayed, M. A. Gold Nanoparticles: Interesting Optical Properties and Recent Applications in Cancer Diagnostic and Therapy. *Nanomedicine* **2007**, *2*, 681–693.
7. Jiang, W.; Kim, B. Y. S.; Rutka, J. T.; Chan, W. C. W. Nanoparticle-Mediated Cellular Response is Size-Dependent. *Nat. Nanotechnol.* **2008**, *3*, 145–150.
8. Michalet, X.; Pinaud, F. F.; Bentolila, L. A.; Tsay, J. M.; Doose, S.; Li, J. J.; Sundaresan, G.; Wu, A. M.; Gambhir, S. S.; Weiss, S. Quantum Dots for Live Cells, *in Vivo* Imaging, and Diagnostics. *Science* **2005**, *307*, 538–544.
9. Roberts, D.; Zhu, W. L.; Frommen, C. M.; Rosenzweig, Z. Synthesis of Gadolinium Oxide Magnetoliposomes for Magnetic Resonance Imaging. *J. Appl. Phys.* **2000**, *87*, 6208–6210.
10. Na, H. B.; Lee, J. H.; An, K. J.; Park, Y. I.; Park, M.; Lee, I. S.; Nam, D. H.; Kim, S. T.; Kim, S. H.; Kim, S. W.; *et al*. Development of a T_1 Contrast Agent for Magnetic Resonance Imaging Using MnO Nanoparticles. *Angew. Chem., Int. Ed.* **2007**, *46*, 5397–5401.
11. Hao, R.; Xing, R.; Xu, Z.; Hou, Y.; Gao, S.; Sun, S. Synthesis, Functionalization, and Biomedical Applications of Multifunctional Magnetic Nanoparticles. *Adv. Mater.* **2010**, *22*, 2729–2742.
12. Louie, A. Multimodality Imaging Probes: Design and Challenges. *Chem. Rev.* **2010**, *110*, 3146–3195.
13. Weissleder, R.; Pittet, M. J. Imaging in the Era of Molecular Oncology. *Nature* **2008**, *452*, 580–589.
14. Jennings, L. E.; Long, N. J. 'Two is Better Than One'-Probes for Dual-Modality Molecular Imaging. *Chem. Commun.* **2009**, *24*, 3511–3524.
15. Cheon, J.; Lee, J. H. Synergistically Integrated Nanoparticles as Multimodal Probes for Nanobiotechnology. *Acc. Chem. Res.* **2008**, *41*, 1630–1640.
16. Kobayashi, H.; Longmire, M. R.; Ogawa, M.; Choyke, P. L. Rational Chemical Design of the Next Generation of Molecular Imaging Probes Based on Physics and Biology: Mixing Modalities, Colors and Signals. *Chem. Soc. Rev.* **2011**, *40*, 4626–4648.
17. Kircher, M. F.; Mahmood, U.; King, R. S.; Weissleder, R.; Josephson, L. A Multimodal Nanoparticle for Preoperative Magnetic Resonance Imaging and Intraoperative Optical Brain Tumor Delineation. *Cancer Res.* **2003**, *63*, 8122–8125.
18. Josephson, L.; Kircher, M. F.; Mahmood, U.; Tang, Y.; Weissleder, R. Near-Infrared Fluorescent Nanoparticles as Combined MR/Optical Imaging Probes. *Bioconjugate Chem.* **2002**, *13*, 554–560.
19. Veiseh, O.; Sun, C.; Gunn, J.; Kohler, N.; Gabikian, P.; Lee, D.; Bhattarai, N.; Ellenbogen, R.; Sze, R.; Hallahan, A.; *et al*. Optical and MRI Multifunctional Nanoprobe for Targeting Gliomas. *Nano Lett.* **2005**, *5*, 1003–1008.
20. Mulder, W. J. M.; Koole, R.; Brandwijk, R. J.; Storm, G.; Chin, P. T. K.; Strijkers, G. J.; Donega, C. D.; Nicolay, K.; Griffioen, A. W. Quantum Dots with a Paramagnetic Coating As a Bimodal Molecular Imaging Probe. *Nano Lett.* **2006**, *6*, 1–6.
21. Wang, S.; Jarrett, B. R.; Kauzlarich, S. M.; Louie, A. Y. Core/Shell Quantum Dots with High Relaxivity and Photoluminescence for Multimodality Imaging. *J. Am. Chem. Soc.* **2007**, *129*, 3848–3856.
22. Beaulac, R.; Schneider, L.; Archer, P. I.; Bacher, G.; Gamelin, D. R. Light-Induced Spontaneous Magnetization in Doped Colloidal Quantum Dots. *Science* **2009**, *325*, 973–976.
23. Magana, D.; Perera, S. C.; Harter, A. G.; Dalal, N. S.; Strouse, G. F. Switching-On Superparamagnetism in Mn/CdSe Quantum Dots. *J. Am. Chem. Soc.* **2006**, *128*, 2931–2939.
24. Lewinski, N.; Colvin, V.; Drezek, R. Cytotoxicity of Nanoparticles. *Small* **2008**, *4*, 26–49.
25. Park, J. H.; Gu, L.; von Maltzahn, G.; Ruoslahti, E.; Bhatia, S. N.; Sailor, M. J. Biodegradable Luminescent Porous Silicon Nanoparticles for *in Vivo* Applications. *Nat. Mater.* **2009**, *8*, 331–336.
26. Tu, C. Q.; Ma, X. C.; Pantazis, P.; Kauzlarich, S. M.; Louie, A. Y. Paramagnetic, Silicon Quantum Dots for Magnetic Resonance and Two-Photon Imaging of Macrophages. *J. Am. Chem. Soc.* **2010**, *132*, 2016–2023.
27. Erogbogbo, F.; Yong, K. T.; Roy, I.; Hu, R.; Law, W. C.; Zhao, W. W.; Ding, H.; Wu, F.; Kumar, R.; Swihart, M. T.; *et al*. *In Vivo* Targeted Cancer Imaging, Sentinel Lymph Node Mapping and Multi-Channel Imaging with Biocompatible Silicon Nanocrystals. *ACS Nano* **2011**, *5*, 413–423.
28. Erogbogbo, F.; Yong, K. T.; Roy, I.; Xu, G. X.; Prasad, P. N.; Swihart, M. T. Biocompatible Luminescent Silicon Quantum Dots for Imaging of Cancer Cells. *ACS Nano* **2008**, *2*, 873–878.
29. Shiohara, A.; Prabakar, S.; Faramus, A.; Hsu, C. Y.; Lai, P. S.; Northcote, P. T.; Tilley, R. D. Sized Controlled Synthesis, Purification, and Cell Studies with Silicon Quantum Dots. *Nanoscale* **2011**, *3*, 3364–3370.
30. Alvarez, S. D.; Derfus, A. M.; Schwartz, M. P.; Bhatia, S. N.; Sailor, M. J. The Compatibility of Hepatocytes with Chemically Modified Porous Silicon with Reference to *in Vitro* Biosensors. *Biomaterials* **2009**, *30*, 26–34.
31. Chin, V.; Collins, B. E.; Sailor, M. J.; Bhatia, S. N. Compatibility of Primary Hepatocytes with Oxidized Nanoporous Silicon. *Adv. Mater.* **2001**, *13*, 1877–1880.
32. Nagesha, D. K.; Whitehead, M. A.; Coffer, J. L. Biorelevant Calcification and Non-Cytotoxic Behavior in Silicon Nanowires. *Adv. Mater.* **2005**, *17*, 921–926.
33. Ruizendaal, L.; Bhattacharjee, S.; Pournazari, K.; Rosso-Vasic, M.; de Haan, L. H. J.; Alink, G. M.; Marcelis, A. T. M.; Zuilhof, H. Synthesis and Cytotoxicity of Silicon Nanoparticles with Covalently Attached Organic Monolayers. *Nanotoxicology* **2009**, *3*, 339–347.
34. Warner, J. H.; Hoshino, A.; Yamamoto, K.; Tilley, R. D. Water-Soluble Photoluminescent Silicon Quantum Dots. *Angew. Chem., Int. Ed.* **2005**, *44*, 4550–4554.
35. Mangolini, L.; Thimsen, E.; Kortshagen, U. High-Yield Plasma Synthesis of Luminescent Silicon Nanocrystals. *Nano Lett.* **2005**, *5*, 655–659.
36. Hessel, C. M.; Henderson, E. J.; Veinot, J. G. C. Hydrogen Silsesquioxane: A Molecular Precursor for Nanocrystalline Si-SiO_2 Composites and Freestanding Hydride-Surface-Terminated Silicon Nanoparticles. *Chem. Mater.* **2006**, *18*, 6139–6146.
37. Atkins, T. M.; Thibert, A.; Larsen, D. S.; Dey, S.; Browning, N. D.; Kauzlarich, S. M. Femtosecond Ligand/Core Dynamics of Microwave-Assisted Synthesized Silicon Quantum Dots in Aqueous Solution. *J. Am. Chem. Soc.* **2011**, *133*, 20664–20667.
38. Zhang, X. M.; Neiner, D.; Wang, S. Z.; Louie, A. Y.; Kauzlarich, S. M. A New Solution Route to Hydrogen-Terminated Silicon Nanoparticles: Synthesis, Functionalization and Water Stability. *Nanotechnology* **2007**, *18*, 095601(1)–095601(6).
39. Manhat, B. A.; Brown, A. L.; Black, L. A.; Ross, J. B. A.; Fichter, K.; Vu, T.; Richman, E.; Goforth, A. M. One-Step Melt Synthesis of Water-Soluble, Photoluminescent, Surface-Oxidized Silicon Nanoparticles for Cellular Imaging Applications. *Chem. Mater.* **2011**, *23*, 2407–2418.
40. Neiner, D.; Chiu, H. W.; Kauzlarich, S. M. Low-Temperature Solution Route to Macroscopic Amounts of Hydrogen Terminated Silicon Nanoparticles. *J. Am. Chem. Soc.* **2006**, *128*, 11016–11017.
41. Rosso-Vasic, M.; Spruijt, E.; van Lagen, B.; De Cola, L.; Zuilhof, H. Alkyl-Functionalized Oxide-Free Silicon Nanoparticles: Synthesis and Optical Properties. *Small* **2008**, *4*, 1835–1841.

42. Clark, R. J.; Dang, M. K. M.; Veinot, J. G. C. Exploration of Organic Acid Chain Length on Water-Soluble Silicon Quantum Dot Surfaces. *Langmuir* **2010**, *26*, 15657–15664.
43. Anthony, R.; Kortshagen, U. Photoluminescence Quantum Yields of Amorphous and Crystalline Silicon Nanoparticles. *Phys. Rev. B* **2009**, *80*, 115407(1)–115407(6).
44. Kelly, J. A.; Veinot, J. G. C. An Investigation into Near-UV Hydrosilylation of Freestanding Silicon Nanocrystals. *ACS Nano* **2010**, *4*, 4645–4656.
45. Veiseh, O.; Gunn, J. W.; Zhang, M. Design and Fabrication of Magnetic Nanoparticles for Targeted Drug Delivery and Imaging. *Adv. Drug Delivery Rev.* **2010**, *62*, 284–304.
46. Castner, T.; Newell, G. S.; Holton, W. C.; Slichter, C. P. Note on the Paramagnetic Resonance of Iron in Glass. *J. Chem. Phys.* **1960**, *32*, 668–673.
47. Harrop, T. C.; Tyler, L. A.; Olmstead, M. M.; Mascharakla, P. K. Change in the Spin State of an Fe-III Center upon One N-to-O Switch in the Coordination of a 2,6-Pyridinedicarboxamido Unit: The Effect of Methyl Thioether and Methyl Ether Appendages at the Ligand Periphery. *Eur. J. Inorg. Chem.* **2003**, *3*, 475–481.
48. Wickman, H. H.; Klein, M. P.; Shirley, D. A. Paramagnetic Resonance of Fe^{3+} in Polycrystalline Ferrichrome A. *J. Chem. Phys.* **1965**, *42*, 2113–2117.
49. Nozaki, C.; Lugmair, C. G.; Bell, A. T.; Tilley, T. D. Synthesis, Characterization, and Catalytic Performance of Single-Site Iron(III) Centers on The Surface of SBA-15 Silica. *J. Am. Chem. Soc.* **2002**, *124*, 13194–13203.
50. Zhilinskaya, E. A.; Delahay, G.; Mauvezin, M.; Coq, B.; Aboukais, A. EPR Investigation of Fe-Exchanged Beta-Zeolites. *Langmuir* **2003**, *19*, 3596–3602.
51. Ferretti, A. M.; Barra, A. L.; Forni, L.; Oliva, C.; Schweiger, A.; Ponti, A. Electron Paramagnetic Resonance Spectroscopy of Iron(III)-Doped MF1 Zeolite. 1. Multifrequency CW-EPR. *J. Phys. Chem. B* **2004**, *108*, 1999–2005.
52. SivaRamaiah, G.; Lin, J. R.; Pan, Y. M. Electron Paramagnetic Resonance Spectroscopy of Fe^{3+} Ions in Amethyst: Thermodynamic Potentials and Magnetic Susceptibility. *Phys. Chem. Miner.* **2011**, *38*, 159–167.
53. Lagarec, K.; Rancourt, D. C. *Recoil, Mössbauer Spectral Analysis Software for Windows, 1.0*; Department of Physics, University of Ottawa: Canada, 1998.
54. Murad, E.; Cashion, J. *Mössbauer Spectroscopy of Environmental Materials and Their Industrial Utilization*; Kluwer Academic Publishers: Dordrecht, The Netherlands, 2004.
55. West, W.; Pearce, S. Dimeric State of Cyanine Dyes. *J. Phys. Chem.* **1965**, *69*, 1894–1903.
56. Armitage, B. A. Cyanine Dye-DNA Interactions: Intercalation, Groove Binding, and Aggregation. In *Topics in Current Chemistry*; Waring, M. J.; Chaires, J. B., Eds.; Springer-Verlag: Berlin, 2005; Vol. 253, pp 55–76.
57. Liu, J.; Yang, X.; Wang, K.; Yang, R.; Ji, H.; Yang, L.; Wu, C. A Switchable Fluorescent Quantum Dot Probe Based on Aggregation/Disaggregation Mechanism. *Chem. Commun.* **2011**, *47*, 935–937.
58. Tu, C.; Ma, X.; House, A.; Kauzlarich, S. M.; Louie, A. Y. PET Imaging and Biodistribution of Silicon Quantum Dots in Mice. *ACS Med. Chem. Lett.* **2011**, *2*, 285–288.
59. Bhattacharjee, S.; de Haan, L. H. J.; Evers, N. M.; Jiang, X.; Marcelis, A. T. M.; Zuilhof, H.; Rietjens, I.; Alink, G. M. Role of Surface Charge and Oxidative Stress in Cytotoxicity of Organic Monolayer-Coated Silicon Nanoparticles Towards Macrophage NR8383 Cells. *Part. Fibre Toxicol.* **2010**, *7*, 25(1)–25(12).
60. Ma, X. C.; Xu, F.; Atkins, T. M.; Goforth, A. M.; Neiner, D.; Navrotsky, A.; Kauzlarich, S. M. A Versatile Low Temperature Synthetic Route to Zintl Phase Precursors: Na_4Si_4, Na_4Ge_4 and K_4Ge_4 as Examples. *Dalton Trans.* **2009**, *46*, 10250–10255.
61. Zou, J.; Sanelle, P.; Pettigrew, K. A.; Kauzlarich, S. M. Size and Spectroscopy of Silicon Nanoparticles Prepared *via* Reduction of $SiCl_4$. *J. Cluster Sci.* **2006**, *17*, 565–578.